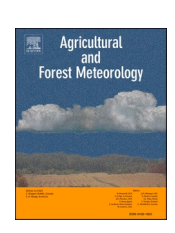
ELSEVIER

Contents lists available at ScienceDirect

Agricultural and Forest Meteorology

journal homepage: www.elsevier.com/locate/agrformet





Models overestimate ecosystem water use efficiency for northern permafrost regions

Jian Wang, Desheng Liu

Department of Geography, The Ohio State University, Columbus, OH 43210, USA

ARTICLE INFO

Keywords:
Permafrost
Ecosystem water use efficiency
Carbon-water coupling
CO₂ fertilization effect
Permafrost-climate feedbacks

ABSTRACT

Understanding the carbon-water coupling over permafrost regions is essential to projecting global ecosystem carbon sequestration and water dynamics. Ecosystem water use efficiency (EWUE), defined as the ratio of gross primary productivity (GPP) and evapotranspiration (ET), reflects plant acclimation strategies with varying ecosystem functioning against environmental stress. Yet EWUE change and its potential drivers across the northern permafrost regions remain poorly quantified, hampering our understanding of permafrost carbon--climate feedback. Here, we compared and analyzed the difference using satellite observations and processbased models to estimate the spatio-temporal variations of EWUE in 1982-2018 over northern permafrost regions. Using flux measurements as truth data, satellite-derived EWUE was more reliable than model-based EWUE. Satellite-derived EWUE showed biome-dependent spatial patterns, with a steady temporal trend (0.01 g C mm $^{-1}$ decade $^{-1}$, P > 0.05) for spatially averaged EWUE over northern permafrost regions. Carbon dioxide (CO₂) concentration and nitrogen deposition positively affected interannual variations of EWUE, while vapor pressure deficit and other climatic factors (i.e., temperature, precipitation, and radiation) negatively controlled EWUE. Compared to satellite-derived EWUE, we found that EWUEs derived from an ensemble of process-based carbon cycle models are overestimated in seven out of ten models, with an increasing trend of 0.11 g C mm⁻¹ $decade^{-1}$ (P < 0.001) for spatially averaged EWUE of the ensemble mean. The relationships between climatic factors and EWUE are partially misinterpreted in model estimates, especially with overstated CO2 sensitivity and the opposite temperature effect. The fluctuating sensitivities to climate over time and the diminishing effect of CO2 fertilization on gross primary productivity (GPP) may partially explain the discrepancy observed between satellite-derived and model-based estimates of EWUE. Thus, this study calls for caution concerning model-based EWUE and aids in understanding permafrost-climate feedbacks and projections of carbon and water cycles.

1. Introduction

Permafrost, covering almost 25% of the land in the Northern Hemisphere, has been experiencing notable degradation under warming, leading to thawing permafrost, rising sea levels, accelerating soil carbon decomposition, and destruction of the ecosystem (Chadburn et al., 2017; Jorgenson et al., 2001; Miner et al., 2021; Plaza et al., 2019). Elevated carbon dioxide (CO₂) concentration, together with climate change and permafrost degradation, substantially alter ecosystem structure and functioning (e.g., shrub expansion across the Arctic) and carbon and water cycles over permafrost regions (Tape et al., 2012; Zhu et al., 2016). Understanding the changes in coupled ecosystem carbon-water dynamics and the underlying mechanism is crucial to projections of plant acclimation and permafrost-climate

feedbacks (Miner et al., 2021; Wu et al., 2021; Yuan et al., 2017).

Terrestrial carbon and water cycles are closely tied to gas exchange through plant stomata (Leuzinger and Körner, 2007; Schlesinger and Jasechko, 2014). Plant water use efficiency (WUE) reflects the resilience and acclimation strategies against environmental stress (e.g., drought, extreme heat, and nutrient stress), linking plant carbon uptake with water consumption from leaf to plant and ecosystem level (Keenan et al., 2013; Yuan et al., 2019). Elevated air CO₂ has been widely reported to enhance leaf 'intrinsic' WUE (iWUE, the instantaneous ratio between carbon assimilation rate and stomatal conductance) across global forests (Battipaglia et al., 2013; Frank et al., 2015; Soh et al., 2019). For example, the iWUE increased by 22% and 14% for coniferous and broadleaf forests during the twentieth century due to elevated CO₂ (Frank et al., 2015). Local- and regional-scale studies, such as

E-mail address: liu.738@osu.edu (D. Liu).

^{*} Corresponding author.

eddy-covariance flux measurements or Free-air CO_2 enrichment (FACE) experiments, confirmed the stimulating effect of CO_2 on WUE for forests (Keenan et al., 2013) and grasslands (Ainsworth and Rogers, 2007). Satellite-based analyses also revealed the positive effects of CO_2 on ecosystem WUE (EWUE), which is defined as the ratio of gross primary productivity (GPP) and evapotranspiration (ET) (Gang et al., 2019; Huang et al., 2015; Zhou et al., 2014).

Apart from CO2 effects, both leaf and ecosystem-level WUE are controlled by other climatic factors, including nitrogen (N) deposition, vapor pressure deficit (VPD), temperature, precipitation, and radiation (Keenan et al., 2013; Huang et al., 2015; Rahman et al., 2019; Xu et al., 2022). For example, drought stress and N deposition have been reported to drive iWUE variations in global forests based on tree ring records, highlighting the demarcation of water-limited from non-water-limited action of leaf stomata (Adams et al., 2021). N deposition stimulates plant growth and nutrient enhancement in plant tissue, enhancing EWUE, especially in N-limited regions (Adams et al., 2021; Brueck, 2008). VPD controls the diurnal and seasonal variations of EWUE and aids in explaining the relationship between GPP and ET across different biomes (Zhou et al., 2014). Using satellite observations and process-based carbon cycle models, Huang et al. (2015) found latitude-dependent responses of climate factors (i.e., temperature, precipitation, and radiation) to EWUE. Temperature, precipitation, and radiation changes may partially or even completely offset the positive CO₂ effects on EWUE (Huang et al., 2015). Specifically, warming and the associated increase in VPD reduce EWUE through substantial increases in ET, as confirmed by modeling and experimental studies (De Boeck et al., 2006; Niu et al., 2011; Querejeta et al., 2021). Precipitation's impacts on EWUE depend upon drought conditions of the ecosystem and soil water storage capacity, showing divergent patterns in arid and humid regions (Tian et al., 2010).

The northern permafrost has been experiencing the release of growing amounts of carbon as a result of degradation caused by warming, which entails higher soil temperatures and an extended duration of annual thawing (Schuur et al., 2015). The increase in carbon release further amplifies climate warming, causing positive permafrost-climate feedbacks, i.e., permafrost carbon feedback (PCF). This positive feedback loop between permafrost thawing and greenhouse gas emissions is a significant concern for climate change as it can accelerate global warming beyond the currently projected levels. A better knowledge of carbon-water coupling could help us understand the mitigating role of vegetation photosynthesis and evapotranspiration processes in PCF. Based on in situ records, flux measurements, and satellite observations, there has been a non-uniform greening trend, with increasing vegetation cover, greenness, and productivity, over northern permafrost regions during the last three decades (Elmendorf et al., 2012; Piao et al., 2020; Zhu et al., 2016). Permafrost greening aids in fixing more carbon from the atmosphere into the ecosystem and mitigates CO2 elevation in the air. Apart from the impacts on carbon uptake, greening over permafrost regions (e.g., Arctic tundra greening) causes biophysical feedbacks to the surface temperature variations, associated with albedo warming and evaporative cooling (Zeng et al., 2017), and water cycles, including increases in ET and precipitation and decreases in runoff and soil moisture (Berner et al., 2020; Piao et al., 2020; Tape et al., 2012). Yet, vegetation impacts on permafrost carbon and water cycles have large uncertainties. Better quantification of EWUE under warming and greening is essential to improve the predictability of future permafrost-climate feedbacks.

Satellite remote sensing has become one of the main approaches to investigating long-term changes in EWUE during the last few decades (Gang et al., 2019; Lu and Zhuang, 2010; Zheng et al., 2019; Zhou et al., 2014). Unlike tree ring isotopes or eddy-covariance flux measurements focusing on individual trees or sites, open-access satellite data can be used to estimate large-scale vegetation dynamics, such as changes in EWUE, with spatial and temporal continuity. Process-based models have also been widely used to determine EWUE (Frank et al., 2015; Huang

et al., 2015). However, their reliability and applicability remain elusive with limited evaluations. Moreover, the climatic responses of model-based EWUE could be biased due to misrepresentation of ecosystem functioning and plant acclimation (Sun et al., 2016). The between-model differences in EWUE can be attributed to different model structures and parameters (Sulman et al., 2012). To this end, this study has threefold goals: (1) to investigate and compare the spatio-temporal patterns of EWUE using satellite observations and model estimations over northern permafrost regions from 1982 to 2018; (2) to understand the dynamic responses of EWUE to changes in climatic drivers; (3) to explain the discrepancy between satellite-derived and model-based EWUE and corresponding climatic sensitivities.

2. Material and methods

2.1. Study area

This study focused on permafrost regions in the Northern Hemisphere, including high-latitude areas such as Siberia, Alaska, and the Canadian Arctic, and high-altitude regions like the Tibetan Plateau. The permafrost coverage was derived from Brown et al. (1997) (Fig. 1). Based on land cover product in 2016 generated by Moderate Resolution Imaging Spectroradiometer (MCD12C1 v006), the Northern permafrost regions are mainly covered by evergreen needleleaf forests (ENF, 7.7%), deciduous needleleaf forests (DNF, 6.1%), mixed forests (MF, 9.7%), open shrublands (OSH, 42.1%), savannas (SAV, 10.9%), grasslands (GRA, 21.2%), and permanent wetlands (WET, 2.3%).

2.2. Datasets

2.2.1. Eddy-covariance flux data

The flux data was collected from FLUXNET (https://fluxnet.org/) over northern permafrost regions. We removed all cropland-site data that was affected by human behaviors. The sites with less than 5-year records were also excluded. Finally, we collected a total of 258 site-year records at 43 sites (Fig. 1). Most of the sites are categorized into ENF (19 sites), GRA (9 sites), and WET (9 sites). Detailed descriptions of flux sites can be seen in Supplementary Table S1. Eddy-covariance-based EWUE was used to evaluate satellite-derived and model-based counterparts in this study.

2.2.2. Satellite-based GPP data

We obtained annual GPP data (1982–2018, $0.05^{\circ} \times 0.05^{\circ}$) from a recent global GPP dataset (GPP_{NIRv}) driven by a satellite-based GPP proxy (i.e., the near-infrared reflectance of vegetation, NIR_V). The NIR_V is calculated as the product of total scene Near-infrared reflectance (NIRT) and the normalized difference vegetation index (NDVI), which are derived from the Advanced Very High Resolution Radiometer (AVHRR). Badgley et al. (2019) illustrated the strong coupling of NIR_V and GPP using flux measurements, even during drought events. The NIR_V approach for estimating GPP achieves strong quantification of uncertainties while maintaining parsimony. GPP_{NIRv} was generated based on calibrated and validated relationships between NIR_V and GPP for different vegetation types, avoiding the integration of climatic factors used as model inputs in other satellite GPP products (Wang et al., 2021).

2.2.3. Determination of ET

By merging estimates from different sources to lower the uncertainty, the triple collocation (TC) method has been widely used to improve the estimates of water cycle components such as precipitation (Li et al., 2018; Lyu et al., 2021), soil moisture (Gruber et al., 2016), snow depth (Xiao and Che, 2018), and ET (Li et al., 2022). Given the largely reported uncertainty of ET estimate (Kingston et al., 2009; Long et al., 2014), we used three independent ET datasets (1982–2018) with the TC method to determine the ET estimate for northern permafrost

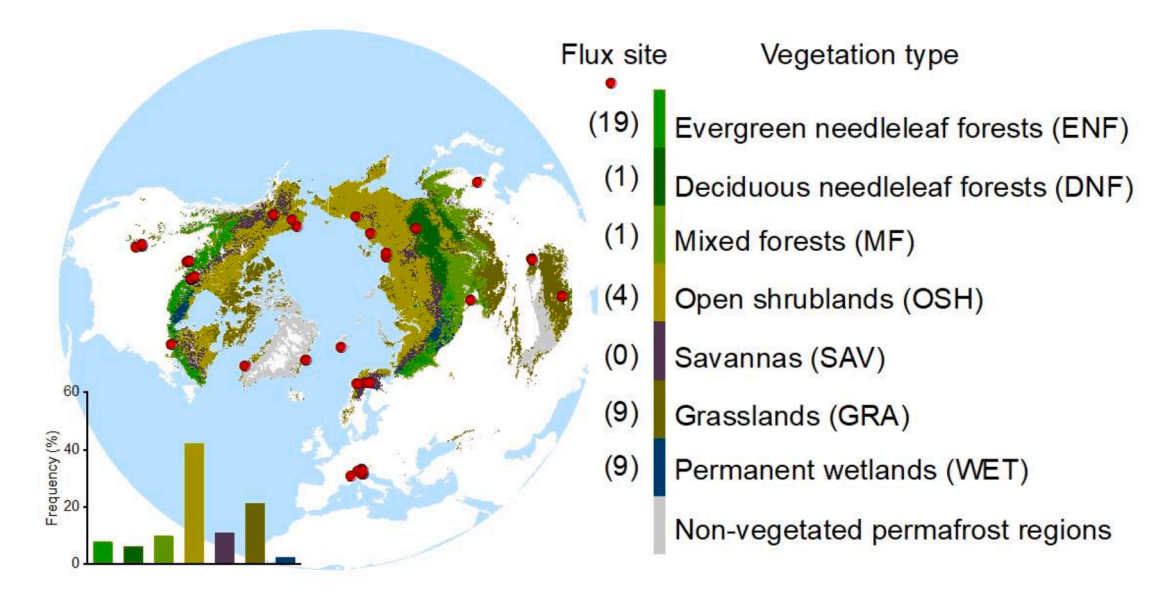


Fig. 1. Distribution of vegetation types and flux sites used in this study over northern permafrost regions.

regions. The first ET dataset is derived from the GLASS ET product (Liang et al., 2020), which is based on a multi-model ensemble approach that merges five process-based ET estimates, i.e., the MODIS ET product algorithm (MOD16) (Mu et al. 2011), the revised remote sensing-based Penman-Monteith ET algorithm (RRS-PM) (Yuan et al. 2010), the Priestley-Taylor-based ET algorithm (PT-JPL) (Fisher et al. 2008), modified satellite-based Priestley-Taylor ET algorithm (MS-PT) (Yao et al. 2013), and the semiempirical Penman ET algorithm of the University of Maryland (UMD-SEMI) (Wang et al. 2010). The second ET dataset is derived from the GLEAM ET product (Martens et al., 2017) using a multiplicative evaporative stress factor and estimates of root-zone soil moisture. The third ET dataset is determined as the residual of the water budget equation (Rodell et al., 2011):

$$ET = P - R - \frac{dTWS}{dt}$$
 (1)

where P is the yearly total precipitation, R is the annual total runoff, TWS is the total water storage, and $\frac{d\text{TWS}}{dt}$ is the annual change in TWS. We used precipitation and runoff data from the TerraClimate dataset (Abatzoglou et al., 2018). Given that the TWS observation based on the Gravity Recovery and Climate Experiment (GRACE) is not available before 2002, we used a reconstructed TWS product for 1982–2018 (Humphrey and Gudmundsson, 2019). All three ET estimates were resampled into $0.05^{\circ} \times 0.05^{\circ}$ as the inputs of the TC method using the bilinear interpolation method.

We conducted the TC method with three main steps (Lyu et al., 2021): (1) determining the RMSEs of the three estimates using the TC analysis; (2) estimating the weight corresponding to each input data; (3) using the weight to calculate weight-averaged ET as the final merged ET. A detailed description of the TC method can be seen in Supplementary Text S1.

2.2.4. Climatic data

We considered six climatic variables, i.e., CO_2 concentration (henceforth, ' CO_2 '), N deposition, VPD, temperature, precipitation, and downward shortwave radiation (henceforth, 'radiation'), as potential drivers of EWUE variations. These six variables are the main factors to impact EWUE variations (Huang et al., 2015). Yearly CO_2 data were collected from a reconstructed monthly gridded atmospheric CO_2 concentrations product under the historical and future scenarios, with a spatial resolution of $1^{\circ} \times 1^{\circ}$ (Cheng et al., 2022). Yearly N deposition data $(0.072727^{\circ} \times 0.072727^{\circ})$ were obtained from Chen et al. (2019),

estimated from tropospheric NO_2 column density. Yearly VPD, temperature, precipitation, and radiation (0.041667° \times 0.041667°) were derived from TerraClimate (Abatzoglou et al., 2018), which have been widely validated with ground observations.

2.3. Process-based models and simulations

We used GPP and ET outputs from ten process-based carbon cycle models based on Trends in the land carbon cycle (TRENDY-v8, released in 2019) project, including CABLE-POP, CLM5.0, DLEM, ISAM, ISBA-CTRIP, LPJ-GUESS, LPX-Bern, ORCHIDEE, SDGVM, and VISIT. The detailed introduction of model information can be seen in Supplementary Table S2. Among multiple simulations of TRENDY-v8, we used simulation S2, which sets up model inputs as varying CO₂, climate, and N deposition with a time-invariant "pre-industrial" land use mask (Huang et al., 2015). Given all process-based models used the same inputs in the TRENDY project, we derived model inputs including CO₂, N deposition, temperature, precipitation, and radiation as climatic drivers of model-based EWUE. To determine VPD, we first derived monthly actual vapor pressure (VAP) and temperature from Climatic Research Unit (CRU TS4.06) dataset. Then we calculated monthly saturated vapor pressure (SVP) as follows (Abbott and Tabony, 1985; Wang et al., 2020):

$$SVP = 0.6107 \times e^{\frac{17.38 \times T}{239.0 + T}}$$
 (2)

where T is the monthly mean temperature. We calculated monthly VPD as the difference between SVP and VAP and then determined yearly mean VPD.

2.4. Statistical analysis

Based on the definition of EWUE, it can be calculated as follows:

$$EWUE = \frac{GPP}{ET}$$
 (3)

where EWUE is annual water use efficiency (g C mm $^{-1}$), GPP is annual total gross primary productivity (g C year $^{-1}$), and ET is annual total evapotranspiration (mm year $^{-1}$).

In this study, we derived three groups of EWUE, i.e., eddy-covariance based EWUE, satellite-derived EWUE, and model-based EWUE. To evaluate satellite-derived and model-based EWUEs by eddy-covariance flux measurements, we applied the bilinear interpolation method to resample model-based EWUE from $0.5^{\circ} \times 0.5^{\circ}$ into $0.05^{\circ} \times 0.05^{\circ}$ to

make it consistent with satellite-derived EWUE. We evaluated EWUEs in terms of correlation coefficient and RMSE. The RMSE was also grouped into different vegetation types. It should be noted that the original coarse resolution of process-based models could partly account for its poor performance of estimating EWUE with insufficient heterogeneity. We performed analyses at two levels (pixel-to-pixel and pixel-aggregated) in order to better interpret the diverse spatial patterns and overall outcomes related to the temporal trends of EWUE and its responses to climatic factors. To investigate climatic responses separately, we resampled climatic drivers into $0.05^\circ \times 0.05^\circ$ for satellite-based analyses and $0.5^\circ \times 0.5^\circ$ for model-based analyses. We used the ensemble mean to represent model-based EWUE and conducted all model-based analyses.

We applied the Theil-Sen slope estimator, a non-parametric and median-based slope estimator, to analyze the temporal trend of satellitederived and model-based EWUEs. The trends were evaluated using the Mann-Kendall trend test at a significance level of 0.05 (Hamed and Rao, 1998). Given multiple climatic factors jointly and interactively influence EWUE, we used partial correlation analysis to investigate the impact of each climatic driver on EWUE variations. To quantitatively describe these impacts, we applied ridge regression to avoid potential multicollinearity among climatic drivers and determine the sensitivity of each driver (i.e., CO2, N deposition, VPD, temperature, precipitation, and radiation). In each grid cell, we determined the dominant factor governing the variations in EWUE as the factor exhibiting the highest absolute sensitivity value (Wang et al., 2022). To investigate the temporal variations of climatic responses, we used an 18-year moving window (15-year and 12-year showed similar results in this study) to determine the changes in sensitivities during the 1982-2018 period.

3. Results

3.1. Evaluations of satellite-derived and model-based EWUEs

Compared to model-based EWUE, satellite-derived EWUE was more promising when evaluated by eddy-covariance flux measurements with a total of 258 site-year EWUE records (Fig. 2). A strong correlation was found between eddy covariance-based EWUE and satellite-derived EWUE, with an R^2 of 0.62 (P < 0.001) and an RMSE of 0.74 g C mm⁻¹ (Fig. 2a). In contrast, model-based EWUE was overall overestimated compared to eddy covariance-based EWUE, with an R^2 of 0.34 (P < 0.001) and an RMSE of 1.09 g C mm⁻¹ (Fig. 2b). Grouping RMSE into vegetation types confirms a better estimation of EWUE using

satellite data, with a lower RMSE than model-based evaluation for each vegetation type.

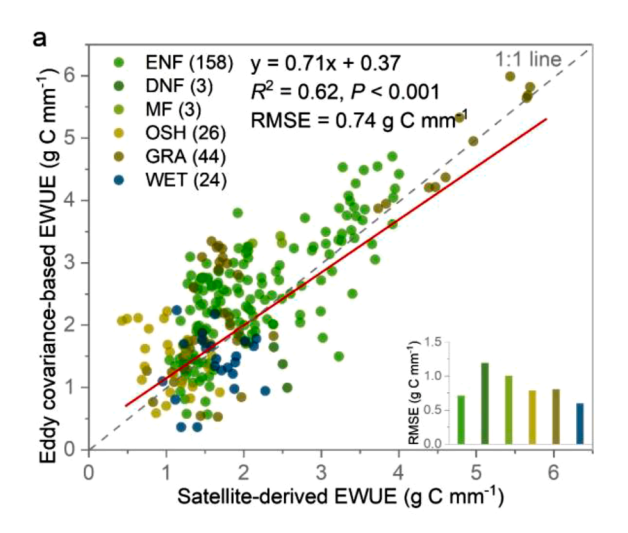
3.2. Spatio-temporal changes in EWUE over northern permafrost regions

Based on satellite-derived EWUE, we observed relatively high EWUE (> 4 g C mm⁻¹) in northwest Canada, Northern Europe, and east of the Tibetan Plateau and low EWUE (< 1 g C mm⁻¹) in the north of Canada and west of the Tibetan Plateau (Fig. 3a). Grouping EWUE into vegetation types shows a biome-dependent distribution of EWUE, ranging from 1.2 \pm 0.5 g C mm $^{-1}$ for OSH to 3.3 \pm 0.9 g C mm $^{-1}$ for SAV (Fig. 3c). We observed high spatial heterogeneity of EWUE trends from 1982 to 2018 over northern permafrost regions (Fig. 3d). Apart from OSH and WET with more increasing trends, EWUEs of ENF, DNF, MF, SAV, and GRA showed no distinct temporal patterns. Overall, 33.2% and 21.6% of the area showed significantly increasing and decreasing trends of EWUE (P < 0.05) (Fig. 3f). Unlike satellite-derived EWUE, modelbased EWUE (i.e., the ensemble mean of all process-based models) showed less spatial heterogeneity in terms of multi-year mean EWUE and EWUE trend (Fig. 3b, d). While relatively high model-based EWUE (> 2.8 g C mm⁻¹) was also found in northwest Canada and Northern Europe, model-based EWUE was overall overestimated compared to satellite-derived EWUE (2.11 vs. 1.68 g C mm⁻¹). Model-based EWUE showed consistent increasing trends for different vegetation types, with a mean value of 0.11 g C mm⁻¹ dec⁻¹ (Fig. 3e, f).

Furthermore, we observed contrasting patterns between satellite-derived estimates and model-based estimates of EWUE when examining spatially averaged values that encompassed all grid cells (Fig. 4). Apart from three process-based models, i.e., DLEM, ISBA-CTRIP, and ORCHIDEE, generating lower EWUE, the remaining seven ensemble models showed higher EWUE compared to satellite-derived EWUE, leading to an overall overestimated ensemble mean EWUE (1.69 vs. 2.05 g C mm $^{-1}$). No distinctive trend of satellite-derived EWUE was observed from 1982 to 2018, while all model-based EWUEs showed increasing trends, with a slope of 0.11 g C mm $^{-1}$ dec $^{-1}$ (P < 0.001) for the ensemble mean EWUE (Fig. 4).

3.3. Responses of EWUE to changes in climatic drivers

We found different partial correlation patterns between satellite-derived EWUE and climatic drivers over northern permafrost regions, covering 7.8% of the area for temperature but 25.8% of the area for CO_2 (P < 0.05) (Fig. 5a). Overall, CO_2 and N deposition had positive-



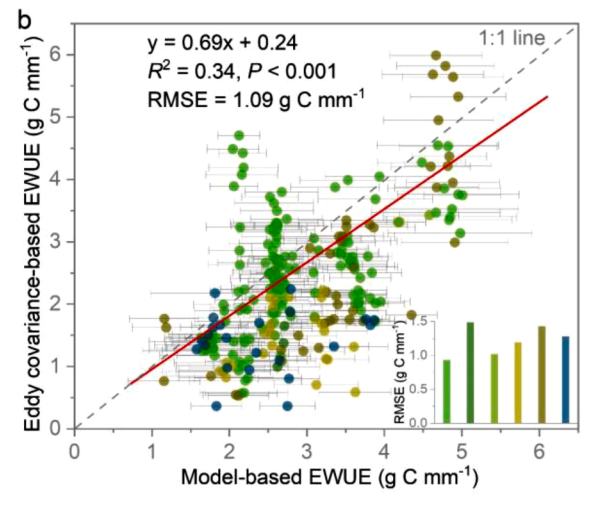


Fig. 2. Evaluations of satellite-derived and model-based EWUEs. The number in the bracket is the total site-year records for each vegetation type. The point and error bar indicates the mean and standard deviation of EWUE derived from an ensemble of process-based carbon cycle models (b). The histograms represent the root mean square error (RMSE) of EWUEs for vegetation types.

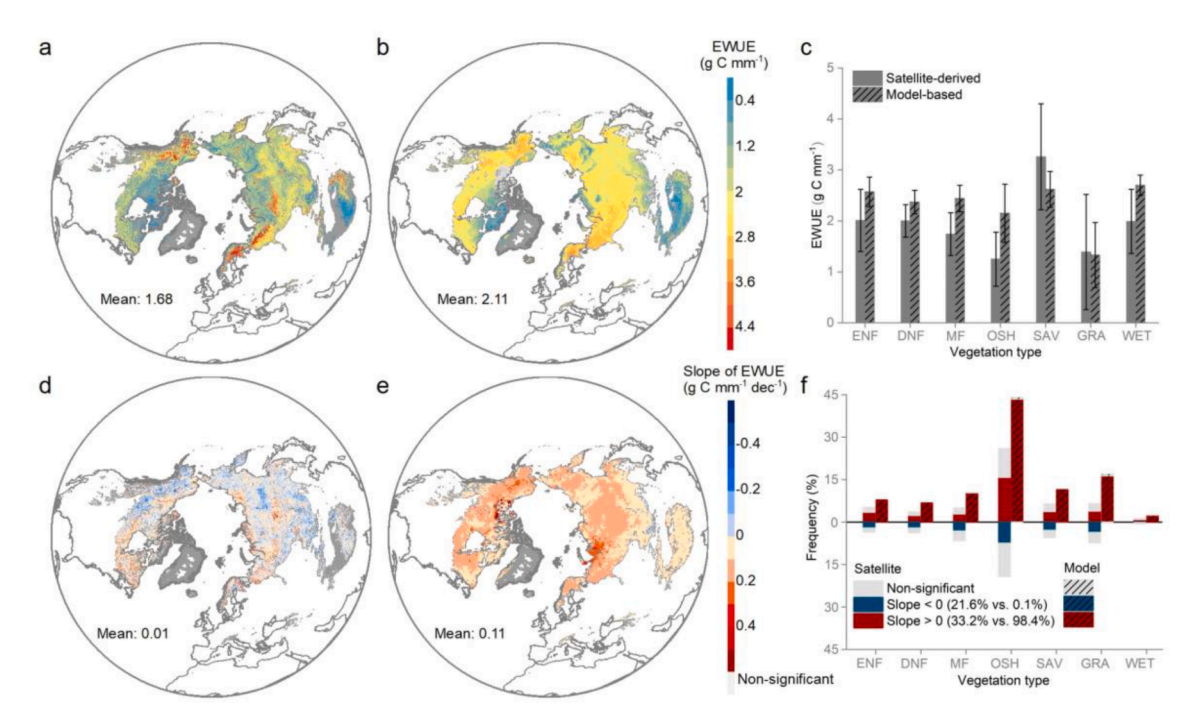


Fig. 3. Spatio-temporal changes in satellite-derived and model-based EWUEs over northern permafrost regions from 1982 to 2018. The model-based EWUE is the ensemble mean EWUE. Spatial variations of multi-year average satellite-derived EWUE (a) and model-based EWUE (b). Distribution of multi-year average EWUEs by vegetation types (c). Temporal trends of EWUE from 1982 to 2018 for satellite-derived EWUE (d) and model-based EWUE (e). Frequency of increasing and decreasing trends of EWUEs by vegetation types (f). The significance of the temporal trend was set as P < 0.05 based on the Mann-Kendall trend test.

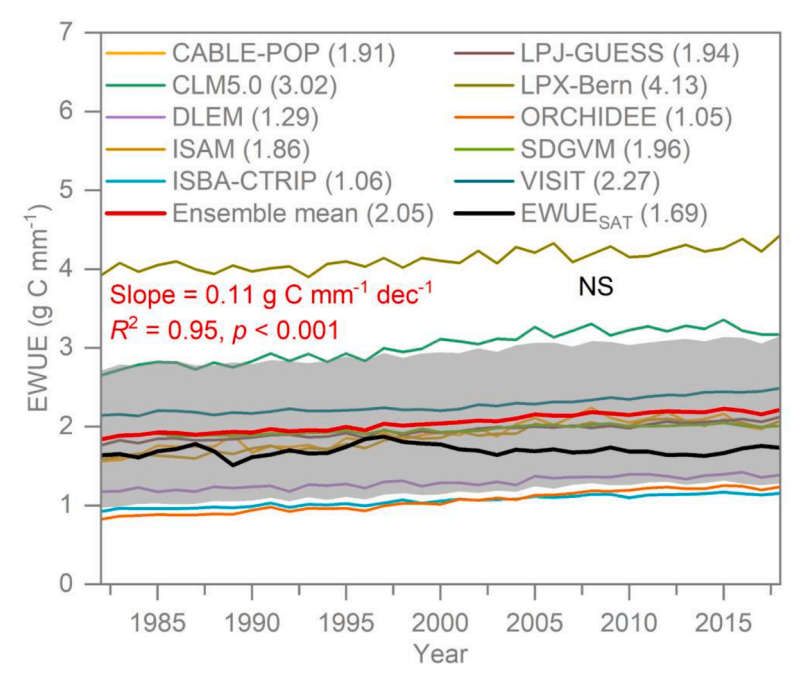


Fig. 4. Comparison of spatially averaged EWUE from satellite observations and model estimates from 1982 to 2018. The value in the basket represents the mean EWUE for the study period. The shaded area indicates the standard deviation of EWUE for all ensemble models.

dominant effects on EWUE, while other drivers, i.e., VPD, temperature, precipitation, and radiation, had negative-dominant impacts. However, a large discrepancy in partial correlation patterns was found in model-based analysis (Fig. 5b). $\rm CO_2$ showed stronger positive impacts on model-based EWUE, and temperature showed contrasting effects compared to satellite-based analysis.

 CO_2 effects dominated nearly half the area for model-based analyses, while this dominance decreased to 20% for satellite-based analyses

(Fig. 6). The negative effects of VPD and radiation on model-based EWUE were underestimated, with the dominance over 9% vs. 16% and 3% vs. 16% in the northern permafrost area, respectively. Process-based models showed discrepant frequencies of dominant drivers, and only one model (SDGVM) exhibited similar $\rm CO_2$ dominance to satellite-based analysis (Fig. 6). Biome-dependent dominance patterns were found for satellite-based analysis (Supplementary Fig. S1). Apart from ENF and WET with more negative dominances mainly from effects of

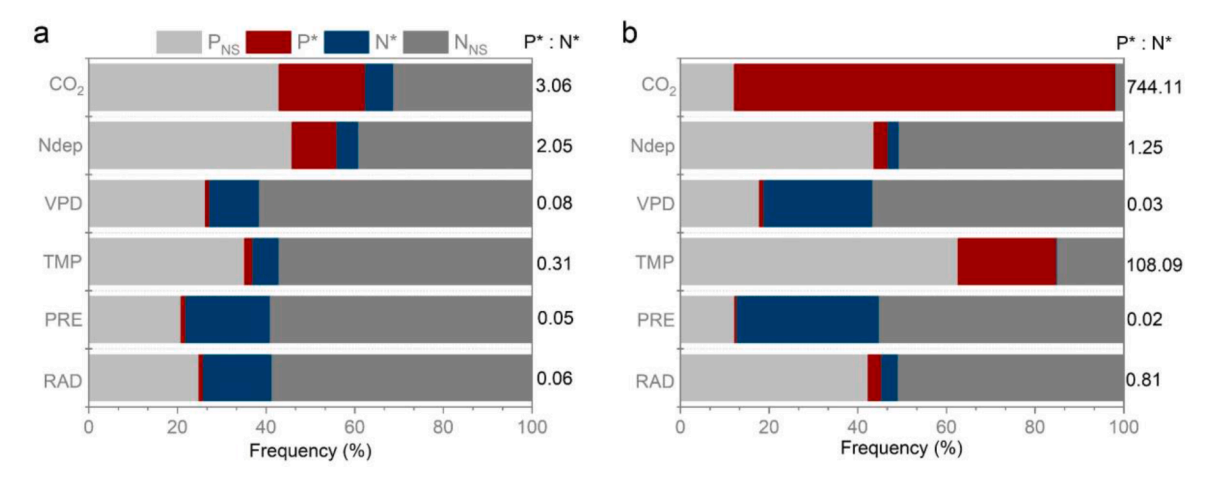


Fig. 5. Distribution of partial correlation coefficients between EWUE and climatic drivers for satellite- (a) and model-based analyses (b). The climatic drivers include CO_2 concentration (CO_2), N deposition (Ndep), vapor pressure deficit (VPD), temperature (TMP), precipitation (PRE), and radiation (RAD). P and N indicate positive and negative correlations, respectively. P* (or N*) and P_{NS} (or N_{NS}) represent significant and non-significant correlations, respectively. The significance was set as P < 0.05. The value on the right side of the stacked bars represents the ratio between significantly positive and negative correlations.

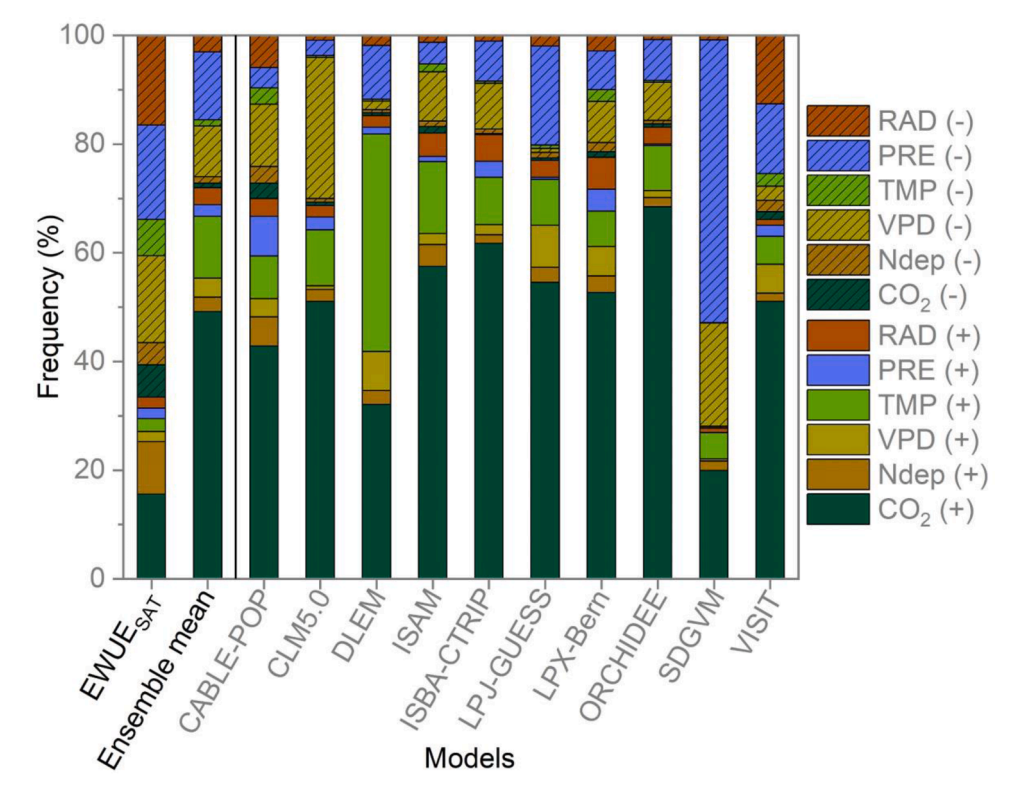


Fig. 6. Frequency of dominant drivers of EWUE for satellite observations (EWUE_{SAT}) and model estimates. The boxes without (with) textiles represent climatic drivers' positive (negative) responses to EWUE variations.

VPD and precipitation, DNF, MF, OSH, SAV, and GRA had more areas with positive dominances from effects of CO₂, N deposition, and temperature.

3.4. Dynamics of EWUE sensitivities and CO₂ fertilization effects

Sensitivity analyses supported the responses of EWUE to climatic drivers, with positive-dominant sensitivities for $\rm CO_2$ and N deposition and negative-dominant sensitivities for VPD, temperature, precipitation, and radiation (Fig. 7). Grouping sensitivities into vegetation types shows the same sensitivities in sign but variant in magnitude for each climatic driver. Apart from radiation with steady sensitivity (negative-dominant,

Fig. 7f), we found decreases in EWUE sensitivities to CO_2 and N deposition (positive-dominant, Fig. 7a, b), decreases in EWUE sensitivities to VPD and precipitation (negative-dominant, Fig. 7c, e), and increases in EWUE sensitivity to temperature (negative-dominant, Fig. 7d). In comparison to climatic sensitivities of satellite-derived EWUE, we found that model-based analyses showed considerably higher sensitivity to CO_2 (0.08 vs. 0.36 \pm 0.07), divergent sensitivities to temperature (-0.06 vs. 0.13 \pm 0.07) and radiation (-0.15 vs. 0.01 \pm 0.05) (Supplementary Fig. S2).

Sensitivities of GPP to CO_2 showed disparate patterns for satelliteand model-based analyses, with a mean value of 0.14 and 0.28, respectively (Fig. 8a, c). Nearly 98% of the area showed a positive effect

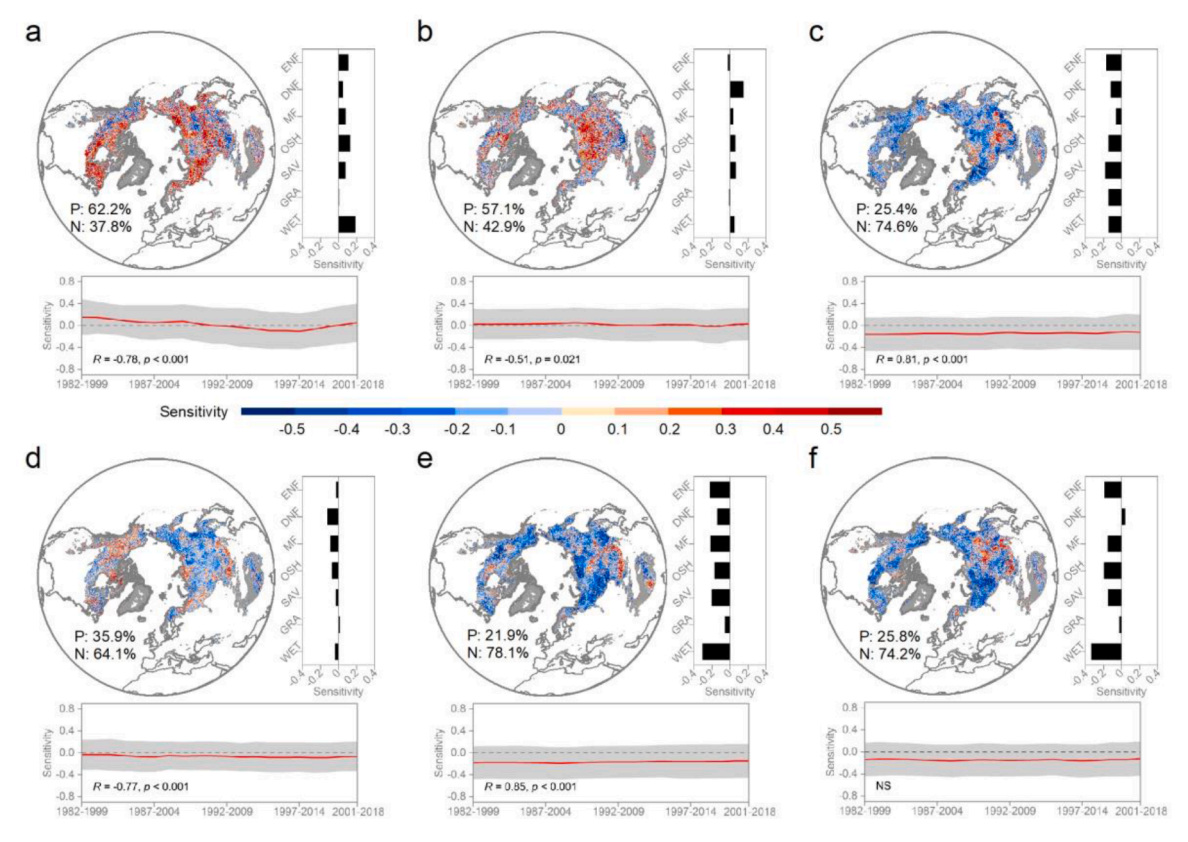


Fig. 7. Sensitivities of satellite-based EWUE to climatic drivers over northern permafrost regions. The climatic drivers include CO_2 concentration (a), N deposition (b), vapor pressure deficit (c), temperature (d), precipitation (e), and radiation (f). The upper right bar indicates the distribution of sensitivities based on vegetation types. The line chart under the map shows the sensitivity variation for each climatic driver using an 18-year moving window. P, N, and NS indicate positive, negative, and non-significant, respectively. The significance was set as P < 0.05.

of CO_2 on the ensemble mean GPP, but it decreased to 69% for satellite-based results. As for temporal trends of the CO_2 fertilization effect, we found a significantly decreasing trend of CO_2 effects for satellite observations (P < 0.001), while no such pattern was observed in model-based analysis over northern permafrost regions (Fig. 8).

4. Discussion

${\it 4.1. \ Spatio-temporal\ patterns\ of\ EWUE\ over\ northern\ permafrost\ regions}$

Changes in EWUE reflect vegetation acclimation confronting varying environmental and climatic conditions (Frank et al., 2015; Huang et al., 2015). Using long-term (1982–2018) satellite-based GPP and improved ET estimates, we found biome-dependent patterns of EWUE over northern permafrost regions (Fig. 3). Herbaceous ecosystems (i.e., OSH and GRA) had lower EWUE than woody ecosystems (i.e., ENF, DNF, and MF) (Fig. 3c), indicating that the coupling of carbon and water is directly controlled by plant root allocation and ecosystem structure (Cramer et al., 2001). Among different vegetation types, the highest EWUE was found in high-latitude SAV, possibly associated with local drought stress and plant acclimation. A thick canopy characterized by a relatively high LAI correlates with elevated GPP and ET. We found higher EWUE in forests than in shrublands and grasslands (Fig. 3c), suggesting the LAI-dependent patterns of carbon-water coupling. A possible physical explanation is that an increase in LAI can significantly diminish soil evaporation by reducing the amount of solar radiation received at the soil surface (Hungate et al., 2002). This progress may offset the greater ET resulting from higher LAI (Huang et al., 2015). High spatial heterogeneity was also observed in the temporal trends of EWUE, even within the same vegetation type (Fig. 3d, f), suggesting the complex and nonlinear responses of EWUE to climate change. Increasing-dominant trends of EWUE in OSH may indicate a tendency for plants to save more water for growth while confronting aggravated drought stress caused by warming and permafrost degradation.

4.2. Responses of EWUE to changes in environment and climate

 ${
m CO_2}$ effects on WUE have been widely reported in leaf-level and ecosystem-level analyses. However, upscaling WUE from the leaf to the ecosystem level is complex because of the impacts of the boundary layer mixing, root allocation, and ecosystem structure (Gentine et al., 2019). Unlike leaf WUE (i.e., iWUE) mainly driven by atmospheric ${
m CO_2}$, EWUE is substantially regulated by climatic conditions. By excluding the effects of other drivers, partial correlation analyses indicate that ${
m CO_2}$ and N deposition positively affect EWUE. In contrast, VPD and climatic factors (i.e., temperature, precipitation, and radiation) showed negative impacts on EWUE (Fig. 5a), which are consistent with previous studies (Adams et al., 2021; Frank et al., 2015; Huang et al., 2015).

Sensitivity analyses confirmed the responses of EWUE to changes in climatic drivers, with overall consistent sensitivity in signs among different vegetation types (Fig. 7). Different patterns of N deposition effects on EWUE were found among forest ecosystems, with strong and slight positive effects for DNF and MF and neutral effects for ENF (Fig. 7b). This divergence could be related to the degree of N limitation to physiology and growth for different forest ecosystems (Adams et al., 2021). Warming enhances vegetation productivity, to some degree, offsetting CO₂ increases globally. However, increases in temperature and associated VPD transfer more water from permafrost to the atmosphere through hydraulic lift under the ground and transpiration by plants (Vereecken et al., 2022), leading to asymmetrical increases in GPP and ET (Supplementary Fig. S3) and lower EWUE (Fig. 7c, d). ET is closely tied to precipitation. For example, ET, as the second largest flux

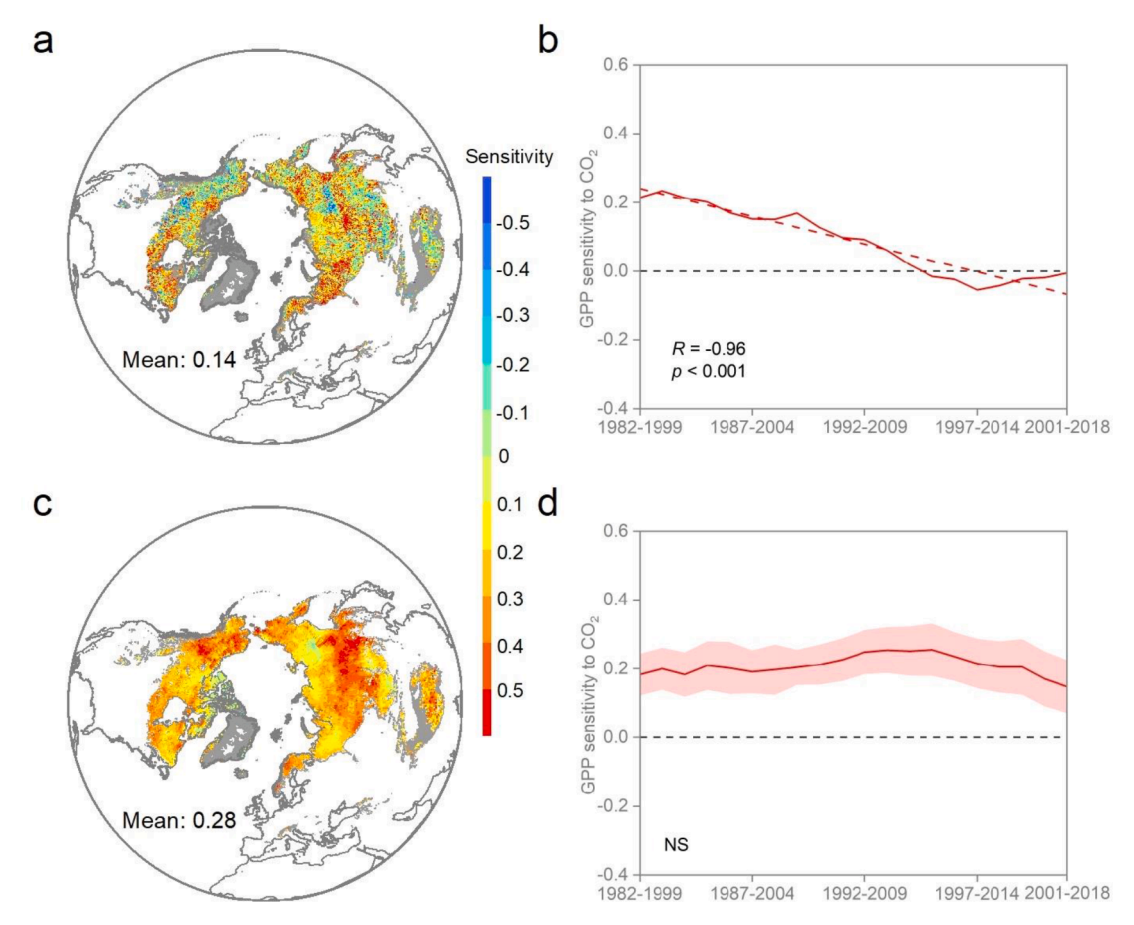


Fig. 8. Responses of GPP to elevated CO_2 for satellite observations and model estimates. Spatial distribution of CO_2 sensitivities to interannual variations of GPP derived from satellite observations (a) and the ensemble mean GPP (c). Temporal variations of CO_2 sensitivities using an 18-year moving window to GPP derived from satellite observations (b) and ensemble mean GPP of process-based models (d). The shaded area indicates the standard deviation of all ensemble models. NS indicates non-significant. The significance was set as P < 0.05.

of the terrestrial water cycle, returns almost 60% of total precipitation into the atmosphere (Jung et al., 2010), exhibiting the strong precipitation control of EWUE with negative sensitivities (Fig. 7e). The partitioning of incident radiation controls latent heat flux (Vereecken et al., 2022), showing strong negative-dominant impacts on EWUE (Fig. 7f). Climatic drivers of EWUE have temporally dynamic effects, with a stronger negative impact of temperature and weaker impacts of $\rm CO_2$, N deposition, VPD, and precipitation on EWUE from 1982 to 2018. The $\rm ^{13}C/^{12}C$ stable isotope ratio in atmospheric $\rm CO_2$ could capture the varying climatic signals to EWUE (Adams et al., 2021). Further investigation in the future is required to enhance our comprehension of the interplay between carbon and water, which is crucial for advancing our understanding in this area.

4.3. Comparisons between satellite-derived and model-based EWUE

Although the scale mismatch might hurt the evaluation of EWUE, we found a better performance of satellite observations in estimating EWUE compared to model estimates (Fig. 2). A large discrepancy between satellite-derived and model-based EWUE estimates was observed over northern permafrost regions, suggesting the limitation of model estimates in coupling ecosystem carbon and water. We found seven out of ten models showed overestimated EWUE, and the ensemble mean EWUE was nearly 20% higher than satellite-derived EWUE (Fig. 4). Model estimates showed consistently increasing trends in EWUE that differ from satellite observation with a stable trend, suggesting the limitation of current process-based models in estimating EWUE variations under varying climatic and environmental conditions.

In addition to the magnitude and trend of EWUE, a substantial difference in EWUE sensitivities was observed between satellite- and model-based analyses, indicating the misrepresentation of climatic responses in model estimates. We found notably overestimated CO2 positive effects, contrasting temperature effect on EWUE for model estimates (Fig. 5). Elevated CO₂ substantially stimulated plant growth and productivity, further regulating the ecosystem coupling of carbon and water globally (Ballantyne et al., 2012; Piao et al., 2020; Schimel et al.,2015). However, changes in temperature and precipitation account for most of the increases in greenness over northern permafrost regions (Zhu et al., 2016), indicating the limitation of CO₂ fertilization effects on GPP and EWUE. Satellite-based analyses in this study have confirmed this limitation. For example, the signal (i.e., the absolute value of EWUE sensitivity) of CO2 was lower than VPD, precipitation, and radiation (Supplementary Figure S3). Unlike the dominance of CO2 (nearly 50%) in model estimates, satellite-based analyses showed limited CO2 control of EWUE variations (less than 20%) (Fig. 6). Meanwhile, satellite-based results showed a decreasing CO₂ fertilization effect on GPP over northern permafrost regions during the last few decades, which has been neglected in model estimates (Fig. 8b, d). A recent study using satellite observations also revealed the global decline of CO2 fertilization effects on plant photosynthesis, explained by the varying nutrient concentrations and soil water availability (Wang et al., 2020). Consistent with our results, model estimates showed a limited capability to capture this decline (Wang et al., 2020). Previous studies illustrated that increases in temperature and radiation regulate carbon uptake and transpiration simultaneously, with a tendency to decrease EWUE due to a stronger elevation of ET (Huang et al., 2015). Thus, the positive effects of temperature and radiation on EWUE (Figs. 5-7) in model estimates reflect that process-oriented models underscore the forcing of temperature and radiation on ET, leading to overestimated EWUE and unexpectedly increasing trends of EWUE across northern permafrost regions. In order to enhance the accuracy of process-based models in estimating EWUE, it is important to focus on integrating dynamic climatic responses, specifically the fluctuations in the CO2 fertilization effect, into the models' structures and parameters.

5. Conclusions

Permafrost is crucial in global carbon and water cycles, but local ecosystem coupling of carbon and water, reflected by EWUE, and its responses to climate change remain elusive. Using satellite-based GPP and improved ET estimates, we quantitatively analyzed the spatiotemporal patterns of EWUE and observed a biome-dependent distribution of EWUE with no distinctive trends from 1982 to 2018 over northern permafrost regions. Both partial correlation and sensitivity analyses showed the positive effects of CO2 and N deposition and the negative effects of VPD, temperature, precipitation, and radiation on EWUE. Moreover, we found an overestimated EWUE with an increasing trend over northern permafrost regions using an ensemble of model estimates, showing the limitation of process-based models in characterizing the coupling of carbon and water. These discrepancies in EWUE estimates may be attributed to the misinterpretation of climatic responses, especially regarding CO₂ fertilization effects on GPP. This study calls for caution concerning model-based EWUE, and future work is needed to improve model processes for projections of vegetation acclimation and permafrost-climate feedbacks.

CRediT authorship contribution statement

Jian Wang: Conceptualization, Data curation, Formal analysis, Investigation, Methodology, Writing – original draft, Writing – review & editing. **Desheng Liu:** Conceptualization, Funding acquisition, Supervision, Writing – review & editing.

Declaration of Competing Interest

The authors declare that they have no known competing financial interests or personal relationships that could have appeared to influence the work reported in this paper.

Data availability

The data link can be seen in Supplementary Table S3. The satellite-based EWUE that supports the findings of this study is available in Zenodo at https://zenodo.org/record/7743136.

Acknowledgments

This study was funded by the National Science Foundation Award (#2126798). We appreciate all public datasets PIs for providing their valuable data for our analyses. The TRENDY-v8 data was requested from Dr. S Sitch and Dr. P Friedlingstein.

Supplementary materials

Supplementary material associated with this article can be found, in the online version, at doi:10.1016/j.agrformet.2023.109594.

References

Abatzoglou, J.T., et al., 2018. TerraClimate, a high-resolution global dataset of monthly climate and climatic water balance from 1958 to 2015. Sci. Data 5, 170191.

- Adams, M.A., et al., 2021. CO₂, nitrogen deposition and a discontinuous climate response drive water use efficiency in global forests. Nat. Commun. 12, 5194.
- Ainsworth, E.A., Rogers, A., 2007. The response of photosynthesis and stomatal conductance to rising CO_2 : mechanisms and environmental interactions. Plant Cell Environ. 30, 258-270.
- Abbott, P.F., Tabony, R.C., 1985. The estimation of humidity parameters. Meteorol. Mag. 114, 49–56.
- Badgley, G_v , et al., 2019. Terrestrial gross primary production: using NIR $_V$ to scale from site to globe. Glob. Change Biol. 25, 3731–3740.
- Ballantyne, A., et al., 2012. Increase in observed net carbon dioxide uptake by land and oceans during the past 50 years. Nature 488, 70–72.
- Battipaglia, G., et al., 2013. Elevated CO₂ increases tree-level intrinsic water use efficiency: insights from carbon and oxygen isotope analyses in tree rings across three forest FACE sites. New Phytologist 197, 544–554.
- Berner, L.T., et al., 2020. Summer warming explains widespread but not uniform greening in the Arctic tundra biome. Nat. Commun. 11, 4621.
- Brown, J., et al., 1997. Circum- Arctic map of permafrost and ground- ice conditions. Washington, DC: U.S. Geological Survey in Cooperation with the Circum- Pacific Council for Energy and Mineral Resources. CircumPacific Map Series CP- 45, scale 1: 10,000,000, 1 sheet.
- Brueck, H., 2008. Effects of nitrogen supply on water-use efficiency of higher plants. J. Plant Nutr. Soil Sci. 171, 210–219.
- Chadburn, S.E., et al., 2017. An observation-based constraint on permafrost loss as a function of global warming. Nat. Clim. Change 7, 340–344.
- Chen, J.M., et al., 2019. Vegetation structural change since 1981 significantly enhanced the terrestrial carbon sink. Nat. Commun. 10, 4259.
- Cheng, W., et al., 2022. Global monthly gridded atmospheric carbon dioxide concentrations under the historical and future scenarios. Sci. Data 9, 83.
- Cramer, W., et al., 2001. Global response of terrestrial ecosystem structure and function to CO₂ and climate change: results from six dynamic global vegetation models. Glob. Change Biol. 7, 357–373.
- De Boeck, G.J., et al., 2006. How do climate warming and plant species richness affect water use in experimental grasslands. Plant Soil 288, 249–261.
- Elmendorf, S.C., et al., 2012. Plot-scale evidence of tundra vegetation change and links to recent summer warming. Nat. Clim. Change 2, 453–457.
- Fisher, J.B., et al., 2008. Global estimates of the land-atmosphere water flux based on monthly AVHRR and ISLSCP-II data, validated at 16 FLUXNET sites. Remote Sens. Environ. 112, 901–919.
- Frank, D.C., et al., 2015. Water-use efficiency and transpiration across European forests during the Anthropocene. Nat. Clim. Change 5, 579–583.
- Gang, C., et al., 2019. Satellite observations of the recovery of forests and grasslands in Western China. JGR Biogeosci. 124, 1905–1922.
- Gentine, P., et al., 2019. Coupling between the terrestrial carbon and water cycles—a review. Environ. Res. Lett. 14, 083003.
- Gruber, A., et al., 2016. Recent advances in (soil moisture) triple collocation analysis. Int. J. Appl. Earth Observ. Geoinform. 45, 200–211.
- Hamed, K.H., Rao, A.R., 1998. A modified Mann-Kendall trend test for autocorrelated data. J. Hydrol. 204, 182–196.
- Huang, M., et al., 2015. Change in terrestrial ecosystem water-use efficiency over the last three decades. Glob. Change Biol. 21, 2366–2378.
 Humphrey, V., Gudmundsson, L., 2019. GRACE-REC: a reconstruction of climate-driven
- water storage changes over the last century. Earth Syst. Sci. Data $11,\,1153-1170$. Hungate, B.A., et al., 2002. Evapotranspiration and soil water content in a scrub-oak
- woodland under carbon dioxide enrichment. Glob. Change Biol. 8, 289–298.

 Jorgenson, M.T., et al., 2001. Permafrost degradation and ecological changes associated
- with a warming climate in central Alaska. Clim. Change 48, 551–579.

 Jung, M., et al., 2010. Recent decline in the global land evapotranspiration trend due to
- limited moisture supply. Nature 467, 951–954. Kingston, D.G., et al., 2009. Uncertainty in the estimation of potential evapotranspiration
- under climate change. Geophys. Res. Lett. 36, L20403. Leuzinger, S., Körner, C., 2007. Water savings in mature deciduous forest trees under
- elevated CO₂. Glob. Change Biol. 13, 2498–2508. Li, C., et al., 2018. Cross-evaluation of ground-based, multi-satellite and reanalysis
- Li, C., et al., 2018. Cross-evaluation of ground-based, multi-satellite and reanalysis precipitation products: applicability of the Triple Collocation method across Mainland China. J. Hydrol. 562, 71–83.
- Li, C., et al., 2022. Error characterization of global land evapotranspiration products: collocation-based approach. J. Hydrol. 612, 128102.
- Liang, S., et al., 2020. The Global LAnd Surface Satellite (GLASS) 1 product suite. Bull. Amer. Meteorol. Soc. 1–37.
- Long, D., et al., 2014. Uncertainty in evapotranspiration from land surface modeling, remote sensing, and GRACE satellites. Water Resour. Res. 50, 1131–1151.
- Lu, X., Zhuang, Q., 2010. Evaluating evapotranspiration and water-use efficiency of terrestrial ecosystems in the conterminous United States using MODIS and AmeriFlux data. Remote Sens. Environ. 114, 1924–1939.
- Lyu, F., et al., 2021. Precipitation merging based on the triple collocation method across mainland China. IEEE Trans. Geosci. Remote Sens. 59, 3161–3176.
- Keenan, T.F., et al., 2013. Increase in forest water-use efficiency as atmospheric carbon dioxide concentrations rise. Nature 499, 324–327.
- Martens, B., et al., 2017. GLEAM v3: satellite-based land evaporation and root-zone soil moisture. Geoscientific Model Devel. 10, 1903–1925.
- Miner, K.R., et al., 2021. Emergent biogeochemical risks from Arctic permafrost degradation. Nat. Clim. Change 11, 809–819.
- Mu, Q., et al., 2011. Improvements to a MODIS global terrestrial evapotranspiration algorithm. Remote Sens. Environ. 115, 1781–1800.
- Niu, S., et al., 2011. Water-use efficiency in response to climate change: from leaf to ecosystem in a temperate steppe. Glob. Change Biol. 17, 1073–1082.

- Piao, S., et al., 2020. Characteristics, drivers and feedbacks of global greening. Nat. Rev. Earth Environ. 1, 14–27.
- Plaza, C., et al., 2019. Direct observation of permafrost degradation and rapid soil carbon loss in tundra. Nat. Geosci. 12, 627–631.
- Querejeta, J.I., et al., 2021. Vertical decoupling of soil nutrients and water under climate warming reduces plant cumulative nutrient uptake, water-use efficiency and productivity. New Phytologist 230, 1378–1393.
- Rahman, M., et al., 2019. Trends in tree growth and intrinsic water-use efficiency in the tropics under elevated CO2 and climate change. Trees 33, 623–640.
- Rodell, M., et al., 2011. Estimating evapotranspiration using an observation based terrestrial water budget. Hydrol. Process 25, 4082–4092.
- Schimel, D., et al., 2015. Effect of increasing ${\rm CO_2}$ on the terrestrial carbon cycle. Proc. Natl. Acad. Sci. 112, 436–441.
- Schlesinger, W.H., Jasechko, S., 2014. Transpiration in the global water cycle. Agric. For. Meteorol. 189-190, 115–117.
- Schuur, E.A.G., et al., 2015. Climate change and the permafrost carbon feedback. Nature 520, 171–179.
- Soh, W.K., et al., 2019. Rising CO_2 drives divergence in water use efficiency of evergreen and deciduous plants. Sci. Adv. 5, eaax7906.
- Sulman, B.N., et al., 2012. Impact of hydrological variations on modeling of peatland CO2 fluxes: results from the North American Carbon Program site synthesis. J. Geophys. Res. Biogeosci. 117, G01031.
- Sun, Y., et al., 2016. Global patterns and climate drivers of water-use efficiency in terrestrial ecosystems deduced from satellite-based datasets and carbon cycle models. Glob. Ecol. Biogeogr. 25, 311–323.
- Tape, K.D., et al., 2012. Landscape heterogeneity of shrub expansion in Arctic Alaska. Ecosystems 15, 711–724.
- Tian, H., et al., 2010. Model estimates of net primary productivity, evapotranspiration, and water use efficiency in the terrestrial ecosystems of the southern United States during 1895-2007. For. Ecol. Manage. 259, 1311–1327.
- Vereecken, H., et al., 2022. Soil hydrology in the Earth system. Nat. Rev. Earth Environ. 3, 573–587.
- Wang, J., et al., 2022. Decreasing rainfall frequency contributes to earlier leaf onset in northern ecosystems. Nat. Clim. Change 12, 386–392.

- Wang, K.C., et al., 2010. Evidence for decadal variation in global terrestrial evapotranspiration between 1982 and 2002: 1. Model development. J. Geophys. Res. 115, D20112.
- Wang, S., et al., 2020. Recent global decline of CO_2 fertilization effects on vegetation photosynthesis. Science 370, 1295–1300.
- Wang, S., et al., 2021. Tracking the seasonal and inter-annual variations of global gross primary production during last four decades using satellite near-infrared reflectance data. Sci. Total Environ. 755, 142569.
- Wu, C., et al., 2021. Widespread decline in winds delayed autumn foliar senescence over high latitudes. Proc. Natl. Acad. Sci. U.S.A. 118 (16), e2015821118.
- Xiao, L., Che, T., 2018. A new comprehensive daily snow depth dataset of the North Hemisphere during 1980-2016 merged from remote sensing, reanalysis, and in situ data based on 'Multiple' collocation. In: Proc. 20th EGU Gen. Assembly, p. 11295.
- Xu, L., et al., 2022. Trends in tree growth and intrinsic water-use efficiency in the tropics under elevated CO2 and climate change. Agric. For. Meteorol. 327, 109188.
- Yao, Y., et al., 2013. MODIS-driven estimation of terrestrial latent heat flux in China based on a modified Priestley-Taylor algorithm. Agric. For. Meteorol. 171, 187–202.
- Yuan, W., et al., 2010. Global estimates of evapotranspiration and gross primary production based on MODIS and global meteorology data. Remote Sens. Environ. 114, 1416–1431.
- Yuan, W., et al., 2017. Influence of vegetation growth on the enhanced seasonality of atmospheric CO₂. Glob. Biogeochem. Cycles 32, 32–41.
- Yuan, W., et al., 2019. Increased atmospheric vapor pressure deficit reduces global vegetation growth. Sci. Adv. 5, eaax1396.
- Zeng, Z., et al., 2017. Climate mitigation from vegetation biophysical feedbacks during the past three decades. Nat. Clim. Change 7, 432–436.
- Zheng, H., et al., 2019. Revegetation has increased ecosystem water-use efficiency during 2000-2014 in the Chinese Loess Plateau: evidence from satellite data. Ecol. Indic. 102, 507–518.
- Zhou, S., et al., 2014. The effect of vapor pressure deficit on water use efficiency at the subdaily time scale. Geophys. Res. Lett. 41, 5005–5013.
- Zhu, Z., et al., 2016. Greening of the Earth and its drivers. Nat. Clim. Change 6, 791–795.